Preferential CO Oxidation in Hydrogen: Reactivity of Core–Shell Nanoparticles

Anand Udaykumar Nilekar,[†] Selim Alayoglu,[‡,§] Bryan Eichhorn,[*,‡] and Manos Mavrikakis[*,†]

Department of Chemical and Biological Engineering, University of Wisconsin–Madison, Madison, Wisconsin 53706, and Department of Chemistry and Biochemistry, University of Maryland, College Park, Maryland 20742

Received February 18, 2010; E-mail: eichhorn@umd.edu; manos@engr.wisc.edu

Abstract: We report on the first-principles-guided design, synthesis, and characterization of core–shell nanoparticle (NP) catalysts made of a transition metal core (M = Ru, Rh, Ir, Pd, or Au) covered with a ~1–2 monolayer thick shell of Pt atoms (i.e., a M@Pt core–shell NP). An array of experimental techniques, including X-ray diffraction, Fourier transform infrared spectroscopy, high resolution transmission electron microscopy, and temperature-programmed reaction, are employed to establish the composition of the synthesized NPs. Subsequent studies of these NPs' catalytic properties for preferential CO oxidation in hydrogen-rich environments (PROX), combined with Density Functional Theory (DFT)-based mechanistic studies, elucidate important trends and provide fundamental understanding of the reactivity of Pt shells as a function of the core metal. Both the PROX activity and selectivity of several of these M@Pt core–shell NPs are significantly improved compared to monometallic and bulk nonsegregated bimetallic nanoalloys. Among the systems studied, Ru@Pt core–shell NPs exhibit the highest PROX activity, where the CO oxidation is complete by 30 °C (1000 ppm CO in H_2). Therefore, despite their reduced Pt content, M@Pt core–shell NPs afford the design of more active PROX catalysts. DFT studies suggest that the relative differences in the catalytic activities for the various core–shell NPs originate from a combination of (i) the relative availability of CO-free Pt surface sites on the M@Pt NPs, which are necessary for O_2 activation, and (ii) a hydrogen-mediated low-temperature CO oxidation process that is clearly distinct from the traditional bifunctional CO oxidation mechanism.

Introduction

As the interest in proton-exchange membrane fuel cell (PEMFC)[1] technology grows, a large number of research studies have focused on alleviating the limitations that prevent broader commercialization of that technology. Of these, production and delivery of clean hydrogen to the PEMFC anode remains one of the most important relevant scientific challenges.[2] Currently, most of the world's industrial hydrogen supply is produced by reforming hydrocarbons. The resulting reformate, although rich in H_2, contains significant amounts of CO, which poisons the surface of the anode catalyst and increases the overpotential for the corresponding reaction.[3,4] A typical sequence for removing CO from reformate includes two stages: (1) water–gas

shift (WGS) reaction[5–8] and (2) preferential oxidation (PROX) of CO.[9] The latter reduces the CO content of reformate down to ppm levels, as needed for stable operation of PEMFCs. Various experimental and theoretical studies have focused on PROX with monometallic,[10–14] alloy,[15–19] and metal oxide[20] catalysts. However, significant improvements in both the activity

(5) Ovesen, C. V.; Stoltze, P.; Nørskov, J. K.; Campbell, C. T. *J. Catal.* **1992**, *134*, 445.
(6) Gokhale, A. A.; Dumesic, J. A.; Mavrikakis, M. *J. Am. Chem. Soc.* **2008**, *130*, 1402.
(7) Grabow, L. C.; Gokhale, A. A.; Evans, S. T.; Dumesic, J. A.; Mavrikakis, M. *J. Phys. Chem. C* **2008**, *112*, 4608.
(8) Farrauto, R. J.; Liu, Y.; Ruettinger, W.; Ilinich, O.; Shore, L.; Giroux, T. *Catal. Rev.—Sci. Eng.* **2007**, *49*, 141.
(9) Ghenciu, A. F. *Curr. Opin. Solid State Mater. Sci.* **2002**, *6*, 389.
(10) Kahlich, M. J.; Gasteiger, H. A.; Behm, R. J. *J. Catal.* **1997**, *171*, 93.
(11) Schubert, M. M.; Kahlich, M. J.; Gasteiger, H. A.; Behm, R. J. *J. Power Sources* **1999**, *84*, 175.
(12) Avgouropoulos, G.; Ioannides, T.; Papadopoulou, C.; Batista, J.; Hocevar, S.; Matralis, H. K. *Catal. Today* **2002**, *75*, 157.
(13) Kandoi, S.; Gokhale, A. A.; Grabow, L. C.; Dumesic, J. A.; Mavrikakis, M. *Catal. Lett.* **2004**, *93*, 93.
(14) Schubert, M. M.; Venugopal, A.; Kahlich, M. J.; Plzak, V.; Behm, R. J. *J. Catal.* **2004**, *222*, 32.
(15) Chin, S. Y.; Alexeev, O. S.; Amiridis, M. D. *J. Catal.* **2006**, *243*, 329.
(16) Schubert, M. M.; Kahlich, M. J.; Feldmeyer, G.; Huttner, M.; Hackenberg, S.; Gasteiger, H. A.; Behm, R. J. *Phys. Chem. Chem. Phys.* **2001**, *3*, 1123.
(17) Ko, E. Y.; Park, E. D.; Lee, H. C.; Lee, D.; Kim, S. *Angew. Chem., Int. Ed.* **2007**, *46*, 734.

[†] University of Wisconsin–Madison.
[‡] University of Maryland.
[§] Present address: University of California, Berkeley, and Lawrence Berkeley National Laboratory, 1 Cyclotron Road, Berkeley, CA 94720.

(1) *Handbook of Fuel Cells—Fundamentals, Technology and Applications*; Wiley: West Sussex, 2003.
(2) Farrauto, R.; Hwang, S.; Shore, L.; Ruettinger, W.; Lampert, J.; Giroux, T.; Liu, Y.; Ilinich, O. *Annu. Rev. Mater. Res.* **2003**, *33*, 1.
(3) Gottesfeld, S.; Zawodzinski, T. A. *Advances in Electrochemical Science and Engineering*; Wiley VCH: Weinheim, Germany, 1997; Vol. 5.
(4) Markovic, N. M. *Handbook of Fuel Cells—Fundamentals, Technology and Applications*; Wiley: Hoboken, NJ, 2003; Vol. 2.

and selectivity of current PROX catalysis are required in order to (1) produce cleaner hydrogen, and thus increase fuel cell performance, and (2) reduce energy consumption for the PROX reaction.

A promising approach for developing improved transition metal catalysts requires a combination of fundamental surface science, experimental studies,[21-27] new NP synthesis methodologies, and first-principles theoretical studies for both analyzing reaction mechanisms and identifying key reactivity descriptors. In prior work aimed at improving PEMFC cathode kinetics, we have shown that, by depositing a Pt monolayer on suitable metal substrates, the reactivity of platinum atoms toward the oxygen reduction reaction (ORR) can be fine-tuned through combined strain and ligand effects.[28-31] These Pt overlayer near-surface alloy (NSA)[32,33] catalysts offer the exciting prospect of achieving higher reactivity while reducing the Pt content of the catalytic NPs.

Here, we report on the first-principles-based design, synthesis, and characterization of Pt*/M, where a monolayer or two of Pt atoms is deposited on one of five different supporting transition metals: Ru, Rh, Ir, Pd, or Au. Since CO poisoning is a major problem for Pt-based PROX catalysts,[10] we first employ density functional theory (DFT) calculations to study the adsorption energetics of CO as a function of its surface coverage, and to estimate the CO saturation coverage on the closest-packed facet of these NSA model surfaces. We then analyze the thermochemistry and kinetics of H_2 dissociation ($H_2 \rightarrow 2H^*$) on these model surfaces as a function of CO coverage to probe their relative reactivity. Subsequently, M@Pt core−shell NPs, which are the synthetic analogues of Pt*/M model systems, are synthesized utilizing polyvinylpyrrolidine (PVP)-based inorganic synthesis protocols. Then, the near-surface elemental composition and PROX activity of various M@Pt catalysts are investigated using an array of experimental techniques, including X-ray diffraction (XRD), fourier transform infrared spectroscopy (FTIR), high-resolution transmission electron microscopy (HR-

TEM), single-particle energy-dispersive X-ray analysis (TEM-EDX), and temperature-programmed reaction (TPR), for catalytic performance evaluation. Among the five M@Pt systems studied, Ru@Pt core−shell NPs show the lowest light-off temperature and most improved PROX properties.[34] Au@Pt is the poorest PROX catalyst and is less active than pure Pt. DFT calculations are used to determine the activation energy barrier for all the elementary steps in the PROX reaction network, so that we can elucidate the fundamental reasons behind the observed reactivity enhancements on M@Pt versus Pt NPs. We suggest that a novel hydrogen-mediated O_2 activation mechanism is responsible for the low-temperature PROX reactivity of these core−shell NPs. The correlation between the calculated activation energy of the CO oxidation step is in excellent agreement with the experimental CO oxidation temperatures on the core−shell NPs, indicating that the DFT-derived PROX reaction mechanism is accurate.

Methods

Theoretical Section. Periodic, self-consistent DFT calculations are carried out using DACAPO,[35,36] a total-energy code. The metal surfaces are modeled using four-layer slabs, with at least five equivalent layers of vacuum separating periodic images of metal slabs in the z-direction of the unit cell. To determine CO saturation coverages and H_2 activation energy barriers in the presence of CO on all surfaces, a $(2\sqrt{3}\times\sqrt{3})$ surface unit cell is employed. To calculate binding energies of various reaction intermediates and the activation energy barriers for elementary steps in the PROX reaction network, a (2×2) unit cell with no spectator CO adsorbates is used. The surface Brillouin zone is sampled using a Chadi−Cohen grid with 18 special k-points in both unit cells. In all cases, convergence with respect to various calculation parameters is confirmed. Adsorption is allowed on only one of the two exposed surfaces of each slab, and the electrostatic potential is adjusted accordingly.[37,38] All degrees of freedom for the top two layers of the slab and for all adsorbate atoms are relaxed. Ionic cores are described by ultrasoft pseudopotentials,[39] and the Kohn−Sham one-electron valence states are expanded in a basis of plane waves with kinetic energy below 25 Ry. The exchange-correlation energy and potential are described self-consistently within the generalized gradient approximation (GGA-PW91).[40,41] The self-consistent PW91 density is determined by iterative diagonalization of the Kohn−Sham Hamiltonian, Fermi population of the Kohn−Sham states ($k_BT = 0.1$ eV), and Pulay mixing of the resulting electronic density.[42] All total energies are extrapolated to $k_BT = 0$ eV. Minimum energy paths and respective transition states for all the elementary reaction steps are identified with the "climbing-image nudged elastic band" method.[43] All transition states are verified by vibrational frequency analysis yielding a single imaginary mode.[44]

The Pt*/M surfaces are modeled by a single layer of platinum atoms placed on top of three-layer slabs of Au(111), Pd(111), Ir(111), Rh(111), or Ru(0001). Accordingly, the Pt overlayer adopts

(18) Watanabe, M.; Uchida, H.; Ohkubo, K.; Igarashi, H. *Appl. Catal., B* **2003**, *46*, 595.
(19) Kim, W. B.; Voitl, T.; Rodriguez-Rivera, G. J.; Evans, S. T.; Dumesic, J. A. *Angew. Chem., Int. Ed.* **2005**, *44*, 778.
(20) Sedmak, G.; Hocevar, S.; Levec, J. *J. Catal.* **2003**, *213*, 135.
(21) Kowal, A.; Li, M.; Shao, M.; Sasaki, K.; Vukmirovic, M. B.; Zhang, J.; Marinkovic, N. S.; Liu, P.; Frenkel, A. I.; Adzic, R. R. *Nat. Mater.* **2009**, *8*, 325.
(22) Stamenkovic, V.; Mun, B. S.; Mayrhofer, K. J. J.; Ross, P. N.; Markovic, N. M.; Rossmeisl, J.; Greeley, J.; Nørskov, J. K. *Angew. Chem., Int. Ed.* **2006**, *45*, 2897.
(23) Tao, F.; Grass, M. E.; Zhang, Y. W.; Butcher, D. R.; Renzas, J. R.; Liu, Z.; Chung, J. Y.; Mun, B. S.; Salmeron, M.; Somorjai, G. A. *Science* **2008**, *322*, 932.
(24) Zhang, J.; Sasaki, K.; Sutter, E.; Adzic, R. R. *Science* **2007**, *315*, 220.
(25) Liu, Z.; Hu, J. E.; Wang, Q.; Gaskell, K.; Frenkel, A. I.; Jackson, G. S.; Eichhorn, B. *J. Am. Chem. Soc.* **2009**, *131*, 6924.
(26) Wang, J. X.; Inada, H.; Wu, L. J.; Zhu, Y. M.; Choi, Y. M.; Liu, P.; Zhou, W. P.; Adzic, R. R. *J. Am. Chem. Soc.* **2009**, *131*, 17298.
(27) Vasquez, Y.; Luo, Z. P.; Schaak, R. E. *J. Am. Chem. Soc.* **2008**, *130*, 11866.
(28) Zhang, J. L.; Vukmirovic, M. B.; Sasaki, K.; Nilekar, A. U.; Mavrikakis, M.; Adzic, R. R. *J. Am. Chem. Soc.* **2005**, *127*, 12480.
(29) Nilekar, A. U.; Xu, Y.; Zhang, J. L.; Vukmirovic, M. B.; Sasaki, K.; Adzic, R. R.; Mavrikakis, M. *Top. Catal.* **2007**, *46*, 276.
(30) Kitchin, J. R.; Nørskov, J. K.; Barteau, M. A.; Chen, J. G. *J. Chem. Phys.* **2004**, *120*, 10240.
(31) Chen, J. G.; Menning, C. A.; Zellner, M. B. *Surf. Sci. Rep.* **2008**, *63*, 201.
(32) Greeley, J.; Mavrikakis, M. *Nat. Mater.* **2004**, *3*, 810.
(33) Knudsen, J.; Nilekar, A. U.; Vang, R. T.; Schnadt, J.; Kunkes, E. L.; Dumesic, J. A.; Mavrikakis, M.; Besenbacher, F. *J. Am. Chem. Soc.* **2007**, *129*, 6485.

(34) Alayoglu, S.; Nilekar, A. U.; Mavrikakis, M.; Eichhorn, B. *Nat. Mater.* **2008**, *7*, 333.
(35) Hammer, B.; Hansen, L. B.; Nørskov, J. K. *Phys. Rev. B* **1999**, *59*, 7413.
(36) Greeley, J.; Nørskov, J. K.; Mavrikakis, M. *Annu. Rev. Phys. Chem.* **2002**, *53*, 319.
(37) Neugebauer, J.; Scheffler, M. *Phys. Rev. B* **1992**, *46*, 16067.
(38) Bengtsson, L. *Phys. Rev. B* **1999**, *59*, 12301.
(39) Vanderbilt, D. *Phys. Rev. B* **1990**, *41*, 7892.
(40) Perdew, J. P.; Chevary, J. A.; Vosko, S. H.; Jackson, K. A.; Pederson, M. R.; Singh, D. J.; Fiolhais, C. *Phys. Rev. B* **1992**, *46*, 6671.
(41) White, J. A.; Bird, D. M. *Phys. Rev. B* **1994**, *50*, 4954.
(42) Kresse, G.; Furthmuller, J. *Comput. Mater. Sci.* **1996**, *6*, 15.
(43) Henkelman, G.; Jónsson, H. *J. Chem. Phys.* **2000**, *113*, 9978.
(44) Greeley, J.; Mavrikakis, M. *Surf. Sci.* **2003**, *540*, 215.

the lattice constant of the respective substrate. The equilibrium PW91 lattice constants for bulk metals are calculated to be 4.18 (Au), 4.00 (Pt), 3.99 (Pd), 3.86 (Ir), 3.85 (Rh), and 2.74 Å (Ru), in good agreement with the respective experimental values[45] [4.08 (Au), 3.92 (Pt), 3.89 (Pd), 3.84 (Ir), 3.80 (Rh), and 2.70 Å (Ru)]. For the Ru hcp lattice, a value of $c/a = 1.582$ is used.

Binding energies (BEs) are calculated as follows: $BE = E_{ads} - E_{clean} - E_{gas}$, where E_{ads}, E_{clean}, and E_{gas} are the total energies of the slab with the adsorbed species on it, the metal slab without adsorbed species, and the adsorbed species in the gas phase, respectively. The differential binding energy (BE_{diff}) for CO is defined as the energy change for the reaction $nCO(a) + \text{surface} + CO(g) \rightarrow (n+1)CO(a) + \text{surface}$. The highest CO coverage for which the differential binding energy of CO is still negative defines the CO saturation coverage on the respective surface. Zero-point energy corrections are small and are not included in this analysis.

Experimental Section. All reactions were carried out under N_2 atmosphere using standard Schlenk line techniques on a Fisher Scientific Isotherm hot plate stirrer with a temperature control unit using a Teflon-coated K-type thermocouple. The colloidal suspensions described below were diluted with acetone and centrifuged at 6000 rpm using a Hermle Z 300. The precipitates were washed with acetone and acetone−ethanol mixtures upon sonication. The cycles of dilution by acetone−ethanol mixtures, sonication, and centrifugation were repeated 4−5 times. The precipitates were dried in open air prior to characterization. Chemicals, $PtCl_2$ (Engelhard, Pt 73.09%), $Pt(acac)_2$ (Strem, 98%, acac = acetylacetonate), $Ru(acac)_3$ (Aldrich, Ru 25.38%), $Rh(NO_3)_3 \cdot 2H_2O$ (Alfa Aesar, 99.9% pure, Rh 31.1%), $RhCl_3$ (Engelhard, Rh 39.46%), $Rh_2(CO)_4Cl_2$ (Fluka, >97%), $HAuCl_4$ (Aldrich, 99.999% pure, Au 57.84% Au), $PdCl_2$ (Engelhard, Pd 60%), $IrCl_3$ (Engelhard, Ir 52.70%), polyvinylpyrrolidine (PVP, Aldrich, typical $M_w = 55\,000$), ethylene glycol (EG, VWR, H_2O >0.02%), acetone (Pharmco Aaper, HPLC-UV grade), $NaBH_4$ (Aldrich, 98% pure, granular), ethanol (Pharmco Aaper, 200 proof), and γ-Al_2O_3 (Alfa Aesar, 99.97% metal basis) were purchased and used as received. The syntheses of Ru@Pt and Rh@Pt catalysts have been described elsewhere.[34,51,52] Details of the analytical methods can be found in the Supporting Information.

Synthesis of Ir@Pt NPs. 2.0 nm Ir NPs. In a typical reaction, 144.6 mg of $IrCl_3$ (0.4 mmol Ir) and 57.1 mg of PVP_{55000} were dissolved in 12 mL of EG in a 50 mL two-neck round-bottom flask at *ca.* 80 °C under flowing N_2. In a separate 100 mL three-neck flask, *ca.* 40 mg $NaBH_4$ was suspended in EG at 100 °C in flowing N_2, and temperature was ramped to 200 °C. The $IrCl_3$ solution was then injected into the $NaBH_4$ solution, giving a black colloidal suspension. While at 200 °C, 500 μL of the 0.02 M NaBr solution in EG was injected into the reaction flask, and the colloidal suspension was refluxed for *ca.* 90 min under flowing N_2. The reaction was quenched on ice. The Ir NP colloids are stable toward precipitation for months.

2.5 nm Ir@Pt (4:5 Ir:Pt) NPs. Typically, 67.4 mg of $PtCl_2$ (0.25 mmol) was dissolved in 18 mL of EG at room temperature in a 50 mL three-neck round-bottom flask under a N_2 atmosphere. An 18 mL portion of the Ir NP suspension described above was transferred using a gastight syringe into the $PtCl_2$ solution at room temperature. The temperature was then ramped to 80 °C to dissolve the $PtCl_2$ salt precursor. Once the $PtCl_2$ was dissolved, the suspension was quickly ramped to 140 °C at a rate of 2−3 °C/min and then slowly brought to 160 °C with a heating rate of 0.5−1 °C/min. Temperature was held at 160 ± 2 °C for 1.5 h and then quenched in an ice bath. The colloids are stable for weeks.

Synthesis of Pd@Pt NPs. 4.0 nm Pd NPs. In a typical reaction, 72.4 mg of $PdCl_2$ (0.4 mmol) and 56.0 mg of PVP_{55000} were dissolved in 10 mL of EG in a 50 mL two-neck round-bottom flask at *ca.* 80 °C under flowing N_2. In a separate flask, *ca.* 20 mg of

granular $NaBH_4$ was suspended in 10 mL of EG at 70 °C. The $PdCl_2$ solution was injected into the $NaBH_4$ solution at 70 °C, which resulted in the instant formation of a black colloid. The resulting mixture was heated to 200 °C and refluxed for *ca.* 120 min under flowing N_2. The reaction was then quenched on ice. The Pd NP colloids are stable for days without precipitation.

4.5 nm Pd@Pt (2:1 Pd:Pt) NPs. Typically, 27.0 mg of $PtCl_2$ (0.1 mmol) was dissolved in 5 mL of EG at room temperature in a 50 mL three-neck round-bottom flask. Following several cycles of vacuuming and N_2-purging, 10 mL of the 4.0 nm Pd colloidal suspension was injected under flowing N_2. The temperature was first ramped to 80 °C to dissolve the $PtCl_2$ salt precursor and then to 120 °C with a ramping rate of 1−2 °C/min. The Pd/Pt suspension was held at 120 ± 2 °C for 120 min and then quenched on ice. The colloids are stable for *ca.* 24 h.

Synthesis of Au@Pt NPs. 2.5 nm Au NPs. Typically, 33.4 mg of $HAuCl_4$ (0.1 mmol Au) and 27.0 mg of PVP_{55000} were dissolved in 30 mL of EG to form a yellow solution at room temperature under nitrogen. The mixture was heated to 60 ± 1 °C. In a separate flask, 80 mg of $NaBH_4$ was dissolved in 10 mL of EG and admitted dropwise into the $HAuCl_4$ solution at 60 °C. The mixture formed a dark purple colloid, which was aged for 120 min at 60 °C and then quenched on ice. The colloids were centrifuged with 20% vol ethanol in acetone and redispersed in 40 mL of EG upon sonication. The redispersed colloids are stable in suspension for weeks.

3.4 nm Au@Pt (3:2 Au:Pt) NPs. In a typical synthesis, 4.7 mg of $PtCl_2$ (0.017 mmol) was dissolved in 10 mL of EG at room temperature. Using a gastight syringe, 10 mL of the Au NP suspension was injected into the $PtCl_2$ solution. The temperature of the solution was quickly ramped to 60 °C and then slowly brought to 100 °C with a temperature ramp of 1−2 °C/min. The Au/Pt suspension was aged at 100 ± 3 °C for 3 h and then quenched in an ice bath. The synthesis of 8.0 nm Au@Pt NPs was conducted in a similar manner and is described in the Supporting Information.

Preparation of γ-Al_2O_3-Supported Catalysts. The M@Pt (M = Ru, Rh, Ir, Pd, and Au) NP catalysts were prepared by adding γ-Al_2O_3 to colloidal suspensions of NPs and drying the slurries under vacuum. The metal loadings were normalized by weight with respect to Pt. For example, 10 mL of Ir@Pt(4:5) NP colloidal suspension and 1.287 g of γ-Al_2O_3 were mixed overnight and dried *in vacuo* at *ca.* 100 °C to give a 1% by weight Pt alumina-supported catalyst. The catalysts were washed with acetone several times and then with an acetone−ethanol mixture (1:1 v/v) twice and then dried at 60 °C for 12 h.

Evaluation of PROX Catalytic Properties. Catalytic reaction runs were carried out using 105 mg of catalyst charges. A standard fixed-bed flow reactor was employed, which has been described elsewhere.[34,46,47] An inlet velocity for gases of 0.21 m/s and a total flow rate of 400 N mL/min were employed. The gas hourly space velocity (GHSV) was calculated to be 2.3×10^5 mL g^{-1} h^{-1}, with a corresponding residence time of about 35 ms. The gas mixture for the 2000 ppm CO PROX reaction was composed of 0.20% CO (99.5% pure, Al tank), 0.5% O_2 (99.999% pure), 50% H_2 (99.999% pure), and balance Ar (99.999% pure). For 1000 ppm CO evaluations, the mixtures were composed of 0.10% CO (99.5% pure, Al tank), 0.5% O_2 (99.999% pure), 50% H_2 (99.999% pure), and balance Ar (99.999% pure). The catalysts were reduced in a 50% H_2−Ar mixture at 200 °C prior to catalytic reaction tests. The temperature was set to 200 °C, and the heating ramp was 1.8 °C/min. The gases were introduced to the reactor using carefully

(45) Ashcroft, N. W.; Mermin, N. D. *Solid State Physics*; Saunders College, Orlando, FL, 1976; Vol. 1.

(46) Zhou, S. G.; McIlwrath, K.; Jackson, G.; Eichhorn, B. *J. Am. Chem. Soc.* **2006**, *128*, 1780.

(47) Zhou, S. H.; Jackson, G. S.; Eichhorn, B. *Adv. Funct. Mater.* **2007**, *17*, 3099.
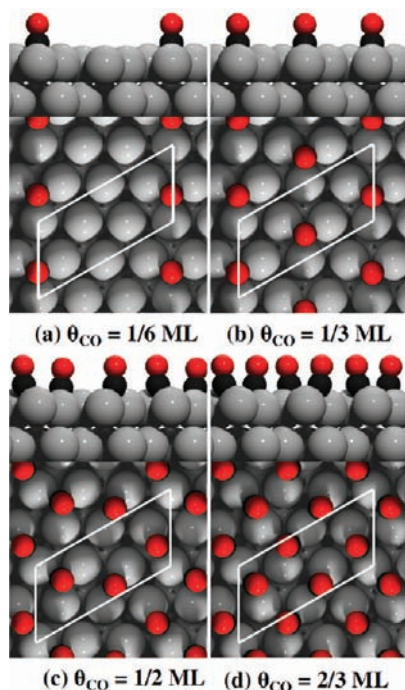
Figure 1. Cross-section and atop views of the optimized geometries of CO adsorbed on Pt(111) at various coverages. Red, black, and gray spheres represent O, C, and Pt atoms, respectively. As a guide to the eye, in the atop views, the unit cell is drawn with white lines.
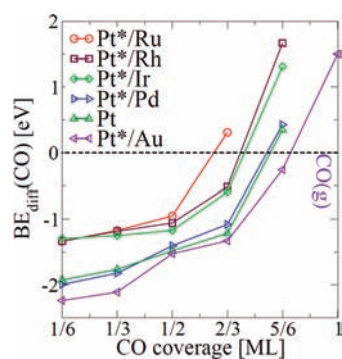

Figure 2. Differential binding energy for CO as a function of CO coverage on various Pt*/M model (111) or (0001) surfaces. A positive differential BE indicates that the respective state is not stable on the surface.

calibrated mass flow controllers. The gas products were monitored online using a Prima δB mass spectrometer.

Results and Discussion

CO Saturation Coverage on Pure Pt and Pt*/M. To calculate the CO saturation coverage on pure Pt and Pt*/M surfaces, the adsorption structure and energetics of CO at different coverages (θ_{CO}) are studied. Figure 1 shows the optimized geometries for CO on Pt(111) at $\theta_{CO} = 1/6$, $1/3$, $1/2$, and $2/3$ monolayer (ML).

The differential binding energies (BE$_{diff}$) of CO on the six surfaces studied are plotted as a function of CO coverage in Figure 2. BE$_{diff}$ decreases with increasing CO coverage for all surfaces, which reflects a weaker binding, because of surface atom sharing and adsorbate−adsorbate repulsion. Thermoneutral adsorption of gas-phase CO is indicated by the horizontal dotted line in Figure 2. For any given surface, the highest CO coverage with a negative BE$_{diff}$ gives the corresponding saturation coverage (θ_{CO}^{sat}) at the limit of low temperatures. For example,

Table 1. CO Saturation Coverage (θ_{CO}^{sat}) and Activation Energy (E_a) for H$_2$ Dissociation on CO-Saturated Pt*/M Surfaces

	θ_{CO}^{sat} (ML)	$E_a(\theta_{CO}^{sat})$ (eV)
Pt*/Ru	1/2	0.85
Pt*/Rh	2/3	2.12
Pt*/Ir	2/3	2.09
Pt*/Pd	2/3	1.54
Pt	2/3	1.40
Pt*/Au	5/6	1.25

on Pt(111), BE$_{diff}$ = −1.93, −1.76, −1.48, −1.21, and +0.35 eV for θ_{CO} = 1/6, 1/3, 1/2, 2/3, and 5/6 ML, respectively. Therefore, adding more CO beyond the 2/3 ML coverage would result in an endothermic process, thus $\theta_{CO}^{sat} = 2/3$ ML for Pt(111). Our calculated value for θ_{CO}^{sat} on Pt(111) is in excellent agreement with a number of experimental studies, including high-pressure STM work for CO on Pt(111).[48,49] We find that Pt*/Pd(111) shows similar CO differential binding energies at all CO coverages, and that Pt*/Pd(111) is characterized by the same CO saturation coverage (2/3 ML of CO) as Pt(111).

At all CO coverages, a Pt monolayer on Ru(0001), Rh(111), or Ir(111) exhibits considerably weaker CO binding as compared to Pt(111) because of both the ligand effect and the compressive strain introduced in the Pt overlayer by the respective substrate.[28–30,32] Although all three surfaces, Pt*/Ru, Pt*/Rh, and Pt*/Ir, have similar BE$_{diff}$ at the lowest θ_{CO} (1/6 ML), they exhibit significantly different behavior at higher CO coverages. Among these three surfaces, Pt*/Ru is the only surface having a θ_{CO}^{sat} lower than 2/3 ML, namely 1/2 ML. Although both Pt*/Rh and Pt*/Ir exhibit weaker CO binding compared to Pt, the CO saturation coverage on these surfaces is 2/3 ML, identical to that on Pt. Among the surfaces studied here, only Pt*/Au shows a stronger BE$_{diff}$ for CO at all coverages when compared to Pt, yielding a $\theta_{CO}^{sat} = 5/6$ ML. This is partly because of the expansive strain induced in the Pt overlayer by the Au substrate. We note here that differences in CO saturation coverage and the BE$_{diff}$(CO) on various surfaces should relate to the relative difficulty in CO removal via oxidation and to the availability of free surface sites for catalytic events. In particular, (i) the lower the CO saturation coverage, the more free surface sites for catalytic events, and (ii) the weaker the binding of CO on a surface, the easier to oxidize it to CO$_2$ on that surface.

Reactivity of CO-Covered Surfaces. Having calculated the CO saturation coverage for these six surfaces, we now proceed with comparing the reactivity of these surfaces as a function of CO coverage. Under realistic PROX conditions, CO will be among the dominant surface species, and therefore probing reactivity as a function of CO coverage is very relevant. For this purpose, we study the thermochemistry and kinetics of H$_2$ dissociation as a function of CO coverage, including the CO-free surface and intermediate coverages up to the saturation coverage of CO spectator species. Accordingly, the activation energy barrier (E_a) and reaction energy (ΔE) as a function of the CO coverage are presented in Table 1 and plotted in Figure 3. The data clearly shows that the reaction energy, $E(2H^*) - E(H_2^*)$ goes from negative to positive values with increasing CO coverage on all surfaces. Since the initial state for this reaction, H$_2^*$, binds very weakly, if at all, the change in the reaction energy reflects the change in binding of atomic

(48) Vestergaard, E. K.; Thostrup, P.; An, T.; Lægsgaard, E.; Stensgaard, I.; Hammer, B.; Besenbacher, F. *Phys. Rev. Lett.* **2002**, *88*, 259601.
(49) Montano, M.; Bratlie, K.; Salmeron, M.; Somorjai, G. A. *J. Am. Chem. Soc.* **2006**, *128*, 13229.
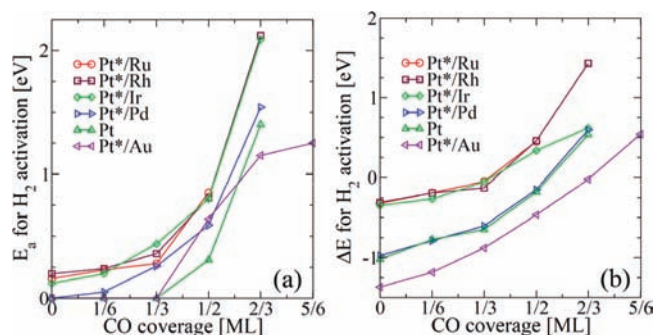
Figure 3. (a) Activation energy barrier (E_a) and (b) reaction energy (ΔE) for H_2 dissociation as a function of CO coverage on Pt*/M and Pt(111) on a four-layered slab in a ($\sqrt{3} \times 2\sqrt{3}$) surface unit cell.

hydrogen as a function of CO coverage. For Pt*/Au, the most stretched surface, the exothermicity of the reaction is retained at all CO coverages, except at the CO saturation coverage (5/6 ML). For Pt*/Pd and Pt, the reaction becomes endothermic at the CO saturation coverage (2/3 ML). For Pt*/Ru, Pt*/Rh, and Pt*/Ir, all of which bind adsorbates more weakly, the reaction becomes endothermic at lower CO coverages (1/2 ML).

For all surfaces studied, the activation energy for H_2 dissociation increases with CO coverage. For instance, H_2 dissociation remains spontaneous ($E_a = 0$ eV) on Pt(111) for $\theta_{CO} = 0$, 1/6, and 1/3 ML. E_a, however, increases to 0.31 and 1.40 eV for $\theta_{CO} = 1/2$ and 2/3 ML, respectively. Therefore, apart from the site-blocking effect introduced by CO coverage, the Pt surface also becomes considerably less reactive: the barrier for H_2 dissociation on the CO-saturated Pt(111) surface is 1.40 eV. One should expect similar increases in activation energy barriers for other bond-breaking reactions, including O_2 dissociation, which is critical for PROX reactivity.[13] This observation can explain the rapid decline in the activity of Pt PROX catalysts at 150 °C[10] and also rationalizes the requirement of higher reaction temperatures for pure Pt-based PROX catalysts, irrespective of the support. The effect of CO coverage on E_a for H_2 dissociation on other surfaces follows a similar trend. Among the surfaces studied (see Table 1), Pt*/Ru(0001) has the lowest CO saturation coverage (1/2 ML) and requires the lowest E_a (0.85 eV) to activate H_2 at that coverage. We note here that this barrier is almost half of that for H_2 dissociation on the CO-saturated Pt(111) surface.

As mentioned already, the strength of CO binding on a surface, which determines the CO saturation coverage, and the activation energy for H_2 dissociation are both important factors determining the *relative* reactivity of these surfaces. For a surface with stronger CO binding energy, it is necessary to increase the reaction temperature to remove some CO from the surface, so that empty sites can be generated for the adsorption/activation of other PROX reactants. As shown above, surfaces with increased CO binding require higher activation energy barriers and thus higher reaction temperatures for some elementary steps to proceed. From Figure 2, one can suggest the following: (1) Pt*/Ru would be the most reactive surface among those considered, since it has the lowest CO saturation coverage (1/2 ML); (2) Pt*/Au would be the least reactive surface, as it shows the highest CO saturation coverage (5/6 ML); and (3) all other surfaces have a 2/3 ML CO saturation coverage. To get an estimate of their relative PROX activity, one can draw a vertical line in Figure 2 at any CO coverage above 1/2 ML, the saturation coverage for Pt*/Ru. On this line, one can rank the surfaces according to differential binding of CO, as follows: Pt

< Pt*/Pd < Pt*/Ir < Pt*/Rh, with Pt and Pt*/Rh showing the strongest and weakest CO binding, respectively. Although differences between a few bimetallics in Figure 2 are small, one could still attempt to derive some qualitative reactivity trends. More specifically, it looks as if the relative PROX reactivity of these six surfaces follows the trend Pt*/Ru > Pt*/Rh > Pt*/Ir > Pt*/Pd > Pt > Pt*/Au. As shown in the following section, this relative PROX activity order is verified when the corresponding M@Pt NP catalysts are tested experimentally. The results reported here show, both qualitatively and quantitatively, that the effect of CO on the reactivity of a catalyst is two-fold: higher CO coverage (1) blocks active sites on the catalytic surface and (2) leads to the destabilization of various adsorbates, resulting in higher activation energies for bond-breaking elementary steps.[50]

Synthesis, Characterization, and PROX Reactivity Studies of M@Pt NPs Synthesis. In this study, 2.5−4.5 nm diameter M@Pt core−shell NPs containing metallic M cores (M = Ru, Rh, Ir, Pd, or Au) and 1.5−2.0 monolayer (ML) thick Pt shells were prepared as direct analogues of the Pt*/M model surfaces described above. The particles were characterized using multiple analytical methods. Representative overviews of the synthesis and characterization of the new catalysts are given here. Details of the methods and results can be found in the Supporting Information and in previous publications (for Ru@Pt and Rh@Pt[34,51,52]).

Monometallic (M) NPs (with M = Ru, Rh, Ir, Pd, or Au) were synthesized by modifications of known glycol methods.[53,54] In the synthesis of all monometallic NP colloids, PVP stabilizers were employed in stoichiometric quantities. The 2.0 nm Ir and 4.0 nm Pd NPs were synthesized via an injection of hot chloride salt solutions into hot NaBH₄ solutions using EG solvents. For the synthesis of Au NPs, the order of addition was reversed. Freshly prepared NaBH₄ solutions were injected into HAuCl₄−PVP solutions in EG at 60 °C. The size of sub-10 nm Au NPs could be controlled and tuned by adjusting the concentration of the NaBH₄ solution. For example, 0.1 M NaBH₄ in EG resulted in *ca.* 5.0 nm Au NPs, and 0.4 M NaBH₄ in EG resulted in *ca.* 2.5 nm Au NPs.

Pt shells of approximately 1−2 ML thicknesses were subsequently deposited on the preformed M (M = Ru, Rh, Ir, Pd, or Au) seeds using a PtCl₂ precursor and seeded growth techniques.[46,55] The PtCl₂ concentrations were adjusted to accommodate the size of the M core particles to achieve 1−2 ML thick Pt shells. A modified form of the Schmid Magic Numbers algorithm for cubo-octahedral clusters and the density of face-centered cubic (or hexagonal close-packed) metal was used to calculate the stoichiometry of M:Pt as described previously.[51] Depositions of the Pt shells on the 2−3 nm NP cores were conducted at temperatures below that of Pt self-nucleation to avoid the formation of monometallic Pt NPs. Uniform spherical particles with Pt coatings were obtained when

(50) Nørskov, J. K.; Bligaard, T.; Logadottir, A.; Bahn, S.; Hansen, L. B.; Bollinger, M.; Bengaard, H.; Hammer, B.; Sljivancanin, Z.; Mavrikakis, M.; Xu, Y.; Dahl, S.; Jacobsen, C. J. H. *J. Catal.* **2002**, *209*, 275.
(51) Alayoglu, S.; Eichhorn, B. *J. Am. Chem. Soc.* **2008**, *130*, 17479.
(52) Alayoglu, S.; Zavalij, P.; Eichhorn, B.; Wang, Q.; Frenkel, A. I.; Chupas, P. *ACS Nano* **2009**, *3*, 3127.
(53) Couto, G. G.; Klein, J. J.; Schreiner, W. H.; Mosca, D. H.; de Oliveira, A. J. A.; Zarbin, A. J. G. *J. Colloid Interface Sci.* **2007**, *311*, 461.
(54) He, B. L.; Chen, Y. X.; Liu, H. F.; Liu, Y. *J. Nanosci. Nanotechnol.* **2005**, *5*, 266.
(55) Habas, S. E.; Lee, H.; Radmilovic, V.; Somorjai, G. A.; Yang, P. *Nat. Mater.* **2007**, *6*, 692.
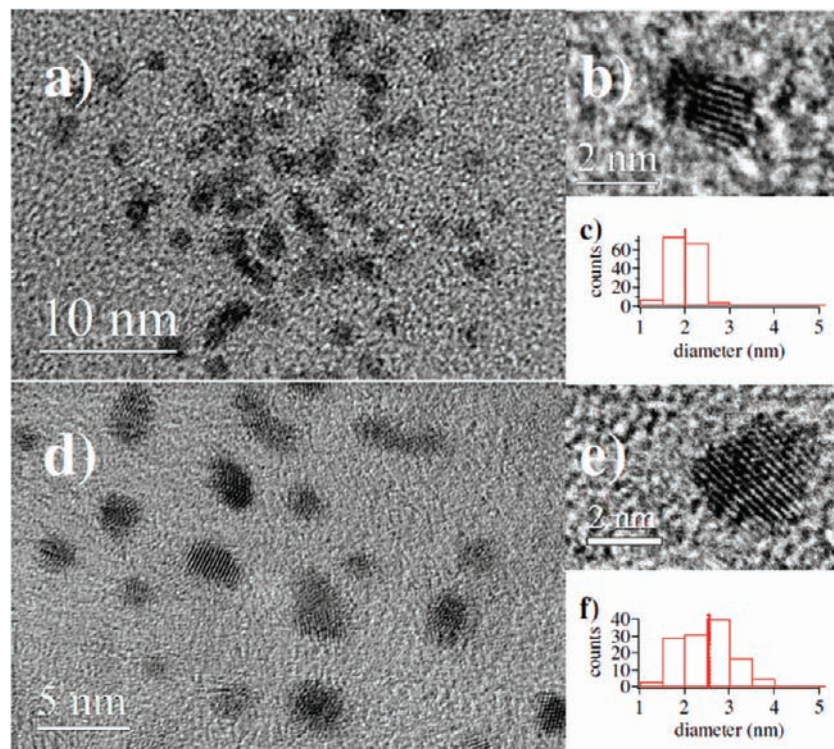
Figure 4. TEM images of (a) Ir NPs and (d) Ir@Pt NPs. HR-TEM images of each are shown in (b) and (e), and size histograms of the particles are shown in (c) and (f), respectively.

deposition temperatures were about 100 °C. For the Au/Pt system, Pt deposition on the 2.5 nm Au cores at temperatures below 100 °C gave spherical, bimetallic core−shell structures, but depositions at 130 °C resulted in mixtures of Au−Pt heteroaggregates, monometallic dimers, and short rods.[47] Above 150 °C, exclusively worm-like wires with alternating Au and Pt fragments were obtained. In contrast, Pt shell growth over the 5.0 nm Au NP seeds was carried out at 130 °C to give uniform 8.0 nm Au@Pt NPs in high yields (see Supporting Information).

Characterization. The NPs described above have been characterized by a combination of TEM, energy-dispersive spectrometry (EDS) single-particle analysis and line scans, XRD, Fourier-transform infrared (FTIR) CO probe measurements, and catalytic evaluations as described below. Representative analyses are given below; more comprehensive descriptions are given in the Supporting Information.

The size evolutions of the core−shell NPs are in agreement with the calculated 1−2 MLs shell thicknesses and thus agree well with the expectations based on the Schmid model (see Figures 4, 5, S1, and S2). While CO probe experiments show that the M (M = Ru, Rh, Ir, or Pd) core particles were completely encapsulated within the Pt shells (see below), the Pt shells described here have variations from particle to particle due to the core size dispersity and growth kinetics of Pt deposition. The size and shell thicknesses reported here are intended to represent only mean values.

The composition and architecture of individual NPs were evaluated using a 1.5 nm EDS probe in JEOL 2100 FE TEM operating in the STEM mode. STEM-EDS line scans were recorded from 8.0 nm Au@Pt NPs with 6.0 nm Au cores and 3−4 ML thick Pt shells (Figures 6 and S3). The data clearly show the Pt L-line with a bimodal Pt distribution that reaches a maximum at the edge of the particle, whereas the Au L-line

shows maximum Au concentration at the center of the particle. While these large particles with thick shells were not employed in the catalysis study below, their larger diameter facilitates line scan analysis and provides a link to the spectroscopic studies of the smaller, catalytically relevant core−shell NPs.

STEM-EDS whole-particle analyses of multiple single particles of the supported 3.4 nm Au@Pt NPs show that each particle has both Pt and Au, with an average Pt:Au ratio of 34:66, which is close to the 40:60 ratio of the precursors (Figure S4). No stray monometallic particles are observed in the samples. Definitive EDS line-scan spectra could not be obtained for the 2.5−5.0 nm M@Pt (M = Ir, Pd, or Au) with 1−2 ML thick Pt shells due to their small size relative to the 1.5 nm STEM probe (Figure S5).

Powder diffraction profiles of monometallic Ir NPs exhibit strong, broad 111 reflections centered at *ca.* 41° in 2θ (Figure S6). The 200 and other high-angle peaks are weak, which denotes a poorly crystalline face-centered-cubic (FCC) phase (i.e., metallic Ir) and is consistent with the TEM images showing the prominent FCC {111} lattice fringes. The X-ray data for the Ir@Pt NPs with *ca.* 1−2 ML thick Pt shells exhibit relatively strong Pt FCC diffraction peaks that are slightly shifted from the bulk peak positions (blue lines in Figure S6). In general, the peaks are slightly shifted to higher 2θ values except for the 200 reflection, which is shifted to lower 2θ. These data are very similar to those of the Ru@Pt NPs,[34] where it was shown that pseudomorphic growth of the Pt shell caused slight strain-induced distortions of the Pt "lattice". A similar change in the Pt structure is likely occurring in the present case.

The XRD data for the 2.5 nm Au NPs show the typical FCC Au phase, whereas the diffraction profiles of the 3.4 nm Au@Pt NPs exhibit both FCC Pt and FCC Au phases (Figure 7). The XRD data clearly rule out the formation of alloy NPs where a single, average FCC structure is observed.[47] Unlike the Ru@Pt,
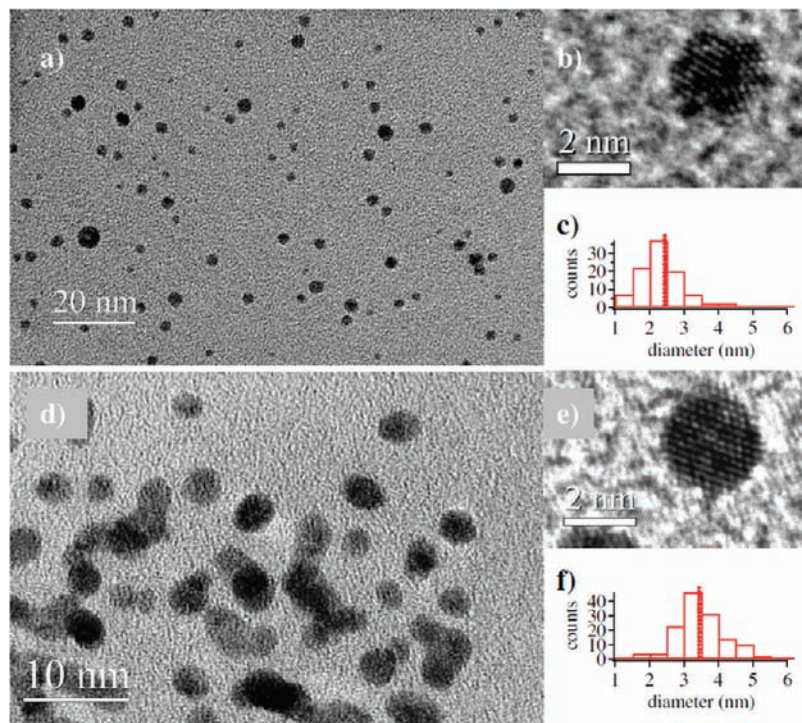
Figure 5. TEM images of (a) 2.5 nm Au NPs and (d) 3.4 nm Au@Pt NPs with ca. 1−2 ML thick Pt shells. HR-TEM images of (b) a 2.5 nm Au icosahedron (e) and a nanocrstalline Au@Pt spheroid are shown, and size histograms of the particles are shown in (c) and (f), respectively.
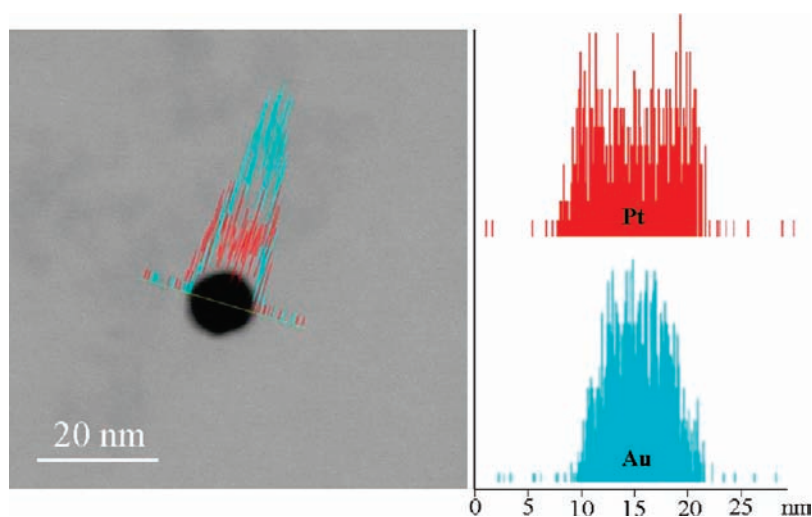

Figure 6. Representative STEM-EDS line spectra of an ∼8.0 nm Au@Pt NP with ∼6.0 nm Au core and 3−4 ML thick Pt shells. Relative atomic % compositions (vertical axis) of Au (blue) and Pt (red) are plotted against the line-scan probe positions (horizontal axis) and are given next to the STEM image. A 1.5 nm probe was used to trace 15−20 nm scans across each particle. The particle center is at ∼15 nm. Representative EDS spectrum is given below the STEM image.

Rh@Pt, and Ir@Pt NPs, the Pt shell diffraction peaks of the Au@Pt NPs are not discernibly shifted from those of bulk Pt, presumably due to the lack of compressive strain in this case.

Because the lattice constants of FCC Pt and Pd are virtually identical ($a_{Pt} = 3.916$ Å and $a_{Pd} = 3.897$ Å), XRD analysis is not a useful tool to distinguish core−shell, alloy, and mono-metallic NPs. The IR CO probe data below are more informative.

Next, we employed CO probe experiments as a qualitative tool to differentiate Pt from M (M = Ir or Pd) on the surface of the particles. To evaluate the surface structure and composition of the various M@Pt (M = Ir or Pd) NPs, the as-prepared NP colloids were dosed with CO and subsequently monitored by FTIR. The infrared spectrum of a physical mixture of mono-
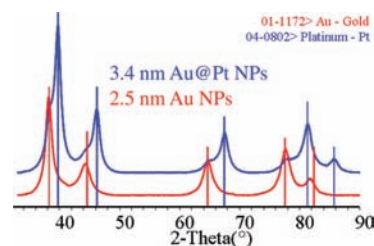

Figure 7. Powder XRD profiles of 2.5 nm Au NPs and 3.4 nm Au@Pt NPs. JCPDS peak positions for Pt (blue) and Au (red) are also presented.
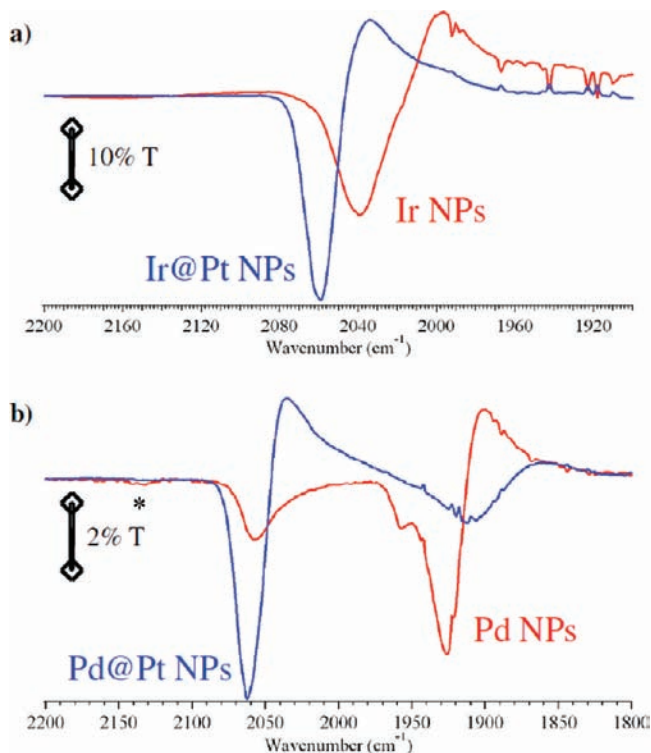
Figure 8. FTIR spectra of CO-saturated colloids of (a) PVP-protected 2.0 nm Ir NPs and PVP-protected 2.5 nm Ir@Pt NPs and (b) 4.5 nm Pd NPs and 5.0 nm Pd@Pt NPs. Asterisk shows free CO in the colloidal suspension. Vertical scale bars show % transmittance (*T*).

metallic Pt and Ir NPs shows the Pt–CO (∼2065 cm^{-1}) and Ir–CO (2040 cm^{-1}) peaks (Figure 8a), which were assigned to the atop adsorption of CO. The infrared spectrum of the Ir@Pt NPs shows a characteristic[34] single symmetric Pt–CO band at 2059 cm^{-1} (Figure 8a), which is distinct from the ν(CO) on monometallic Ir NPs.

The infrared spectrum of the CO-saturated colloids of monometallic Pd NPs (Figure 8b) shows both linear and bridging binding modes of the adsorbed CO. The weak 2050 cm^{-1} peak is assigned to an atop ν(CO) on Pd and the strong peak at 1930 cm^{-1} to a bridging ν(CO) on Pd. After Pt deposition at monolayer coverage, a single strong peak shows up at 2060 cm^{-1}, along with a broad, weak feature at 1900 cm^{-1}. The former is attributed to atop ν(CO) on Pt and the latter to bridging ν(CO), both on the electronically altered Pt surface sites. The CO probe technique has also been used to spectroscopically monitor the formation of the Pt shell in the synthesis of the Pd@Pt NPs. The colloidal suspension of NPs was sampled at various times during the reaction and evaluated by FTIR. The terminal ν(CO) band associated with the Pd NPs blue-shifts and increases in intensity as the linear CO bands associated with CO adsorbed to the Pt surface emerge (see Figure S7). To demonstrate the sensitivity of FTIR monitoring of CO adsorption on Pt and Pd surfaces, Pd was successively deposited over the Pd@Pt NPs to form double-shell Pd@Pt@Pd NPs with 1–2 ML thick Pt shells sandwiched between Pd cores and 1–2 ML thick Pd shells. These NPs show ν(CO) bands that are characteristic of Pd surface sites.

PROX Reaction Studies. The catalytic activities of the 2–4.5 nm M@Pt (M = Ru, Rh, Ir, Pd, or Au) core–shell NPs were evaluated for preferential oxidation of CO in H$_2$ fuel streams (PROX). The M@Pt NPs were loaded onto γ-Al$_2$O$_3$ supports such that each catalyst contained 1.0 wt % Pt. The catalysts
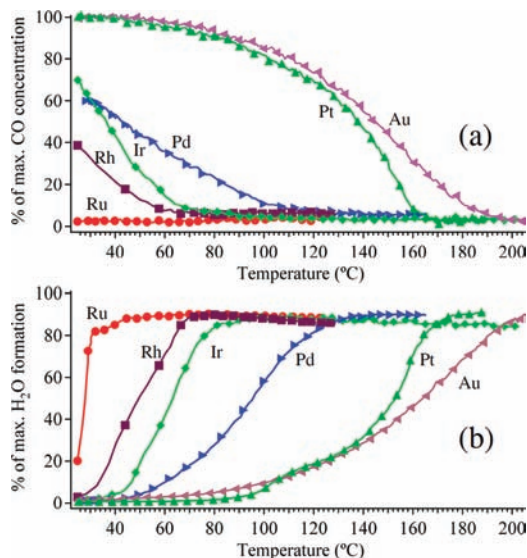

Figure 9. TPR plots for the PROX reaction showing (a) CO concentration and (b) H$_2$O formation at a CO level of 1000 ppm, for the M@Pt (M = Ru, Rh, Ir, Pd, or Au) core–shell NPs with ca. 1 ML thick Pt shells and the 2.5 nm Pt particle catalysts.
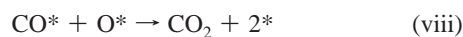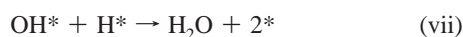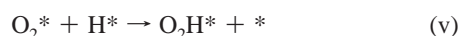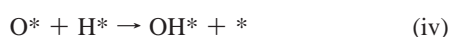
were initially screened using a PROX feed composed of 1000 ppm CO, 5000 ppm O$_2$, 50% H$_2$, and balance Ar. Because the core–shell nanoparticles have 1–2 ML thick Pt shells, similar particle sizes and were normalized by Pt content, the total surface area of any catalyst charge is approximately equal. For example, the 2.5 nm Ir@Pt particles, 1.0% by weight Pt supported in γ-Al$_2$O$_3$, had a TEM-projected surface area of *ca.* 1.5 × 10^3 m^2/g and a number density of *ca.* 2.0 × 10^{20} NPs per gram of the catalyst. Similarly, the 4.5 nm Pd@Pt particles, 1.0% by weight Pt supported in γ-Al$_2$O$_3$, had a TEM-projected surface area of *ca.* 1.4 × 10^3 m^2/g but a lower number density of *ca.* 0.4 × 10^{20} NPs per gram of the catalyst due to the larger diameter of the NPs relative to Ir@Pt. Therefore, the observed trends in PROX activity and selectivity directly reflect surface reactivity.

For 1000 ppm CO, the PROX activities decreased in the order of Ru@Pt > Rh@Pt > Ir@Pt > Pd@Pt > Pt > Au@Pt. Furthermore, all showed H$_2$ oxidation subsequent to CO oxidation (Figure 9), except for the Au@Pt NPs catalyst, where H$_2$ and CO oxidations occurred simultaneously (Figure 9). For 2000 ppm CO, the relative order in PROX activities was retained with minor differences between the samples (see Figure S8). Importantly, the Au@Pt NPs catalyst has a lower activity than pure Pt and exhibited only partial CO oxidation at complete O$_2$ consumption. We can describe the different behaviors by defining limiting chemical equations for oxidation in mixed CO/H$_2$ feeds. In a perfect PROX reaction (eq 1), CO oxidation is 100% selective and H$_2$ is unreacted. In the other limit, which can be termed "CO-tolerant" behavior, hydrogen is selectively oxidized in the presence of CO (eq 2). Most activities are intermediate between these two limits but can be classified by their approach to a given limiting behavior. For example, the Au@Pt NPs show CO-tolerant behavior with very low selectivities for PROX, especially at high CO concentrations. In contrast, the Ru@Pt, Rh@Pt, and Ir@Pt systems are far more selective for CO oxidation and are superior PROX catalysts.

PROX: $$CO + H_2 + 1/2O_2 \rightarrow CO_2 + H_2 \qquad (1)$$
CO-tolerant: $$CO + H_2 + 1/2O_2 \rightarrow CO + H_2O \qquad (2)$$
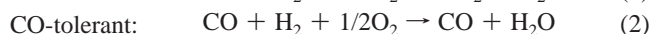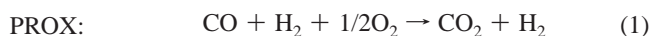
At 1.0% CO concentrations, the Ir@Pt and Rh@Pt catalysts exhibit better selectivity than the Ru@Pt NPs (Figure S9). CO selectivity ranged between ~90% at low temperatures for partial O_2 conversions and ~55% at high temperatures for complete O_2 conversions. The Au@Pt NPs exhibited the lowest activity and selectivity among all studied at any given temperature and CO partial pressure.

PROX Reaction Mechanism. Although there are a number of prior experimental studies corroborating the effect of CO coverage on various reactions,[10,56−59] to our knowledge, the exact mechanistic aspects of that effect have not been investigated. To explain the relative PROX reactivity of various M@Pt NPs, we consider the detailed reaction mechanism. In particular, in our DFT calculations we account for the following elementary reaction steps:

$$H_2 + 2* \rightarrow 2H* \qquad \text{(i)}$$

$$O_2 + * \rightarrow O_2* \qquad \text{(ii)}$$

$$O_2* + * \rightarrow 2O* \qquad \text{(iii)}$$

$$O* + H* \rightarrow OH* + * \qquad \text{(iv)}$$

$$O_2* + H* \rightarrow O_2H* + * \qquad \text{(v)}$$

$$O_2H* + * \rightarrow O* + OH* \qquad \text{(vi)}$$

$$OH* + H* \rightarrow H_2O + 2* \qquad \text{(vii)}$$

$$CO* + O* \rightarrow CO_2 + 2* \qquad \text{(viii)}$$

where * indicates a surface site.

It should be noted that, apart from the elementary steps in the traditionally accepted PROX mechanism,[10] we include steps v and vi, representing the formation of a hydroperoxy (O_2H*) intermediate via hydrogenation of O_2* and its dissociation into $O*$ and $OH*$. The motivation for including these two additional steps comes as a result of (1) our experimental observation that CO oxidation rates on Pt are higher in the presence of H_2 than in its absence and (2) the lack of experimental evidence for such a "promotional" effect in the presence of H_2O.[10,34] The thermochemistry and kinetics of all elementary steps i−viii are investigated on all six Pt*/M model surfaces with a (2×2) surface unit cell. Simple inspection of the above reaction network suggests that the PROX activity and selectivity of a surface will depend on its ability to (1) generate surface $O*$ through either direct or H-mediated O_2 dissociation (steps iii, or v followed by vi, respectively), (2) remove CO through its oxidation (step viii), and (3) remove the remaining surface O through H_2O elimination (steps iv followed by vii, and vi followed by vii).

The binding energies of all relevant species in the PROX reaction network on all six surfaces (see Table S1 in the Supporting Information) are plotted in Figure 10a. Atomic oxygen ($O*$) and hydrogen ($H*$) exhibit the strongest binding among all species, and the magnitude of their binding energy increases in the following order: Pt*/Ru < Pt*/Rh < Pt*/Ir <
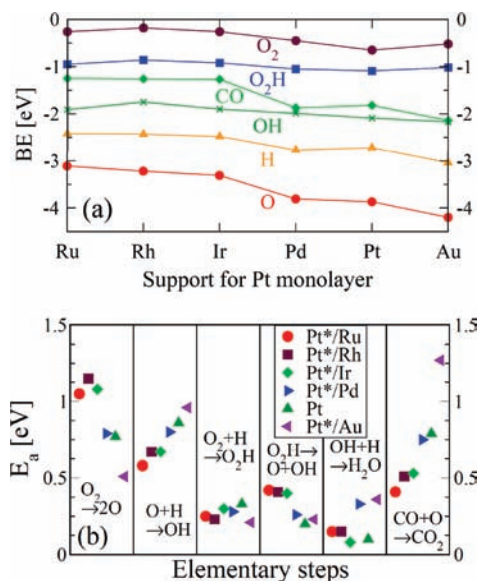

Figure 10. (a) Binding energy (BE) of different reaction intermediates and (b) activation energy (E_a) for different PROX elementary steps on clean Pt*/M and Pt(111) on four-layer slabs with a (2×2) surface unit cell.

Pt*/Pd < Pt < Pt*/Au. Hydroxyl ($OH*$), hydroperoxy (O_2H*), and molecular oxygen (O_2*) all show smaller variations in their binding energies from one surface to the next. As discussed earlier (see Figure 2), the binding energy of CO shows significant variation on the six surfaces. Accordingly, these variations reflect modifications in the electronic structure of the Pt overlayer induced by the supporting metal surface through strain and the ligand effect.[30,32,60] It is worth noting that the relative trends of $CO*$ and $H*$ binding energies calculated for the bare surfaces reported in Figure 10a mirror those for binding energies of $CO*$ and $H*$ on CO-covered surfaces (Figures 2 and 3b). Therefore, the *relative* ordering of reactivity of these surfaces can be established even without accounting for higher CO spectator coverage. This is important, as inclusion of CO spectator species in our calculations leads to a substantial increase in computational cost. Thus, we used the bare (2×2) surfaces for the forthcoming detailed analysis of the PROX reaction network.

The activation energies of bond-breaking/making PROX elementary steps iii−viii (see Table S1 in the Supporting Information) are shown in Figure 10b. The activation energy for bond-breaking steps (reactions iii and vi) decreases as the final state of the respective step is stabilized.[28,61] Accordingly, the activation energy for bond-making steps (reactions iv, v, vii, and viii) generally increases as the surface stabilization of the reactant species increases.[50] These trends are much more pronounced for direct O_2 dissociation (step iii), $O* + H* \rightarrow OH*$ (step iv), and $CO* + O* \rightarrow CO_2$ (step viii).

To analyze the relative activity of the Pt*/M surfaces for generating surface $O*$, we compare the activation energies for steps iii, v, and vi. The direct O_2 dissociation step iii has the highest activation energy on Pt*/Ru, Pt*/Rh, and Pt*/Ir, with barriers greater than 1 eV, which decreases progressively on Pt*/Pd, Pt, and Pt*/Au. Therefore, in the absence of H_2, CO oxidation proceeds via this difficult O_2 dissociation step on all

(56) Li, Q. F.; He, R. H.; Gao, J. A.; Jensen, J. O.; Bjerrum, N. J. *J. Electrochem. Soc.* **2003**, *150*, A1599.

(57) Camara, G. A.; Ticianelli, E. A.; Mukerjee, S.; Lee, S. J.; McBreen, J. *J. Electrochem. Soc.* **2002**, *149*, A748.

(58) Gasteiger, H. A.; Markovic, N. M.; Ross, P. N. *J. Phys. Chem.* **1995**, *99*, 8945.

(59) Bartholomew, C. H. *Appl. Catal., A* **2001**, *212*, 17.

(60) Greeley, J.; Mavrikakis, M. *Catal. Today* **2006**, *111*, 52.

(61) Xu, Y.; Ruban, A. V.; Mavrikakis, M. *J. Am. Chem. Soc.* **2004**, *126*, 4717.

surfaces and results in lower reaction rates on Pt*/Ru, Pt*/Rh, and Pt*/Ir as compared to those on Pt*/Pd, Pt, and Pt*/Au. However, in the presence of H_2, we find that the H-mediated O_2 dissociation mechanism (steps v and vi) is very easy on all surfaces. On all six surfaces atomic H* addition to O_2* leads to the formation of a hydroperoxy intermediate (O_2H*) with small barriers ($E_a < 0.35$ eV). The hydroperoxy intermediate (O_2H*) then decomposes into O* and OH*, again with fairly small barriers on all surfaces ($E_a < 0.42$ eV). Therefore, we suggest that in H_2-rich PROX reaction environments, surface O* is primarily generated through the H-assisted O_2 dissociation mechanism. Importantly, this suggestion can also explain the experimentally observed enhancement of CO oxidation rates induced by the presence of H_2.[10]

The activation energy for CO* + O* → CO_2 (step viii) characterizes the ability of the surface to remove CO via oxidation. We find that the CO oxidation barrier increases progressively in the order Pt*/Ru < Pt*/Rh < Pt*/Ir < Pt*/Pd < Pt < Pt*/Au, which closely tracks the trend discussed earlier for the binding energy and saturation coverage of CO as a function of the identity of the surface (Pt*/M). The stronger the binding of CO and O to the surface, the more activated the CO oxidation step becomes. Therefore, among those studied, Pt*/Ru emerges as the best surface for CO oxidation. In addition, since O* formation through the H-mediated mechanism is very easy on all these surfaces, our theoretical mechanistic studies clearly suggest that Pt*/Ru should be the most active PROX surface among those studied here.

The alternative route for removing O* from the surface is via H_2O formation, which is achieved through steps iv and vii. As shown in Figure 10b, the barrier for step iv (O* + H* → OH*) follows the same trend as that for CO oxidation, whereas further hydrogenation of OH to H_2O (reaction vii) is a rather easy step, with $E_a < 0.4$ eV on all surfaces studied.

Overall, since direct O_2* dissociation can be circumvented through the H-mediated O_2* activation on all surfaces, CO oxidation and OH formation are energetically the most difficult steps on all six surfaces. The relative energetics of these two steps dictates both their relative activity and selectivity for PROX. The barrier for each of these two steps increases in the following order: Pt*/Ru < Pt*/Rh < Pt*/Ir < Pt*/Pd < Pt < Pt*/Au, and accordingly reflects the PROX relative *activity* of these surfaces. This relative activity order is in excellent agreement with the experimentally observed trends for the experimentally measured temperature at which 50% of CO_2 formation is achieved (T_{50}). Furthermore, on all these surfaces, with the exception of Pt*/Au, CO oxidation has a smaller barrier than OH formation O* + H* → OH*, resulting in higher selectivity for CO rather than hydrogen oxidation. As shown in Figure 11, the plot of theoretically calculated activation energies for the CO_2 formation step versus the experimental T_{50} values exhibits excellent quantitative agreement; i.e., with increasingly difficult CO_2 formation, the T_{50} increases. This agreement indicates that first-principles approaches can be used to identify the key PROX reactivity descriptors and to identify and design the most promising core−shell nanoparticles, prior to engaging in the tedious synthesis of those NPs for arbitrary bimetallic compositions.

Conclusions

Using a combination of first-principles calculations and experiments, we have systematically examined the PROX reactivity of specifically synthesized and characterized M@Pt
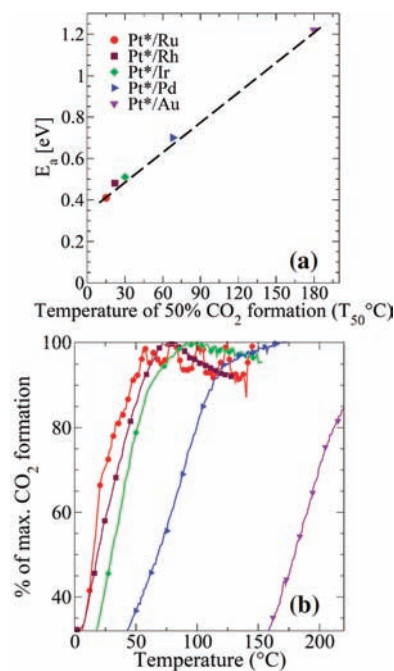

Figure 11. (a) Activation energies, E_a, for the reaction step of CO oxidation on the Pt*/M model surfaces plotted against the temperatures of 50% CO_2 formation on the core−shell M@Pt (M = Ru, Rh, Ir, Pd, or Au). (b) TPR plots for the PROX reaction showing CO_2 formation at 2000 ppm CO level on the core−shell NPs.

NPs, made of various transition metal cores (Ru, Rh, Ir, Pd, Au) covered by a ca. 1−2 monolayer thick shell of Pt atoms. Among these nanoparticles, the PROX reactivity is the highest for Ru@Pt core−shell NPs, followed by Rh@Pt, Ir@Pt, Pd@Pt, pure Pt, and Au@Pt NPs, in order of decreasing reactivity. The Ru@Pt core−shell NPs are more active than their constituent pure metal NPs, as well as their conventional nanoalloys.[34]

The absolute value of the binding energy of CO, a key poison for Pt PROX catalysts, on these surfaces increases in the following order: Ru@Pt < Rh@Pt < Ir@Pt < Pd@Pt < Pt < Au@Pt, which indicates a progressively increasing difficulty in removing CO from the surface through either oxidation or desorption. We show that improvements in PROX activity of Pt monolayers on various supporting metals are directly related to weakening of; to the decreasing absolute value the CO binding energy on the Pt surface. Ru@Pt core−shell NPs, in particular, exhibit the weakest CO binding, leading to the lowest CO saturation coverage, 1/2 ML, and the maximum PROX reactivity. The other extreme is represented by Au@Pt core−shell NPs, where CO binds the strongest, leading to the highest CO saturation coverage, 5/6 ML, and the minimum PROX reactivity. The relative differences in the T_{50} values for CO oxidation to CO_2 versus H_2 oxidation to H_2O on these NPs are also rationalized by the differences in activation energy barriers for the respective competing elementary steps.

Thus, DFT calculations in combination with PROX catalytic experiments on specifically synthesized core−shell NPs have identified two key properties for the development of improved PROX catalysts: (1) relative trends in the CO adsorption behavior, which, in turn, govern the CO saturation coverage, and (2) the relative difficulty of CO oxidation versus H_2O formation on the Pt*/M surfaces. Finally, our suggestion for the H-mediated O_2 activation on catalytic surfaces can explain the enhanced low-temperature CO oxidation activity in the presence of H_2. These results present yet another example of

the interplay between experimental and theoretical studies guiding the development of improved catalysts through a fundamental understanding of catalytic chemistry at the atomic scale.

Supporting Information Available: Additional details for TEM, STEM-EDS, XRD, FTIR, and TPR experiments and theoretical calculations (Figures S1−S9 and Table S1). This material is available free of charge via the Internet at http://pubs.acs.org.

JA101108W